Atmospheric
Chemistry
and Physics
Discussions

Aerosol and cloud properties in the Namibian region during AEROCLO-sA field campaign: 3MI airborne simulator and sun-photometer measurements.

Aurélien Chauvigné[1], Fabien Waquet[1], Frédérique Auriol[1], Luc Blarel[1], Cyril Delegove[1], Oleg Dubovik[1], Cyrille Flamant[2], Marco Gaetani[2,3,6], Philippe Goloub[1], Rodrigue Loisil[1], Marc Mallet[4], Jean-Marc Nicolas[1], Frédéric Parol[1], Fanny Peers[5], Benjamin Torres[1], and Paola Formenti[6].

[1] Univ. Lille, CNRS, UMR 8518 - LOA - Laboratoire d'Optique Atmosphérique, F-59000 Lille, France.
[2] LATMOS, UMR CNRS 8190, Sorbonne Université, Université Paris-Saclay, Institut Pierre Simon Laplace, Paris, France.
[3] Scuola Universitaria Superiore IUSS, Pavia, Italy.
[4] CNRM, Université de Toulouse, Météo-France, CNRS, Toulouse, France.
[5] CEMPS, University of Exeter, Exeter, EX4 4QE, UK.
[6] LISA, UMR CNRS 7583, Université Paris-Est-Créteil, Université de Paris, Institut Pierre Simon Laplace, Créteil, France.

Correspondence to: Aurélien Chauvigné (aurelien.chauvigne@univ-lille.fr)

Abstract. We analyse of the airborne measurements of above-cloud aerosols from the AEROCLO-sA field campaign performed in Namibia during August and September 2017. To improve the retrieval of the aerosol and cloud properties, the airborne demonstrator of the Multi-viewing, Multi-channel, Multi-polarization (3MI) satellite instrument, called OSIRIS, was deployed on-board the Safire Falcon 20 aircraft during 10 flights performed over land, over the ocean and along the Namibian coast. The airborne instrument OSIRIS provides observations at high temporal and spatial resolutions for AAC and cloud properties, with well-defined uncertainties. OSIRIS was supplemented with the airborne multi-wavelength sun-photometer PLASMA2. The application of the algorithm developed for the POLDER spaceborne instrument in the visible range to the OSIRIS measurements allowed to characterise the Aerosol Above Cloud (AAC) properties. The variations of the aerosol properties are consistent with the different atmospheric circulation regimes observed during the deployment. Airborne observations typically a show strong Aerosol Optical Depth (AOD, up to 1.2 at 550 nm) of fine mode particles from biomass burning (extinction Angström exponent varying between 1.6 and 2.2), transported above a stratocumulus deck (cloud top around 1 km above mean sea level) with Cloud Optical Thickness (COT) up to 35 at 550 nm. The above-cloud visible AOD retrieved with OSIRIS agrees within 10 % with the PLASMA2 sun-photometer measured in the same environment.

The AEROCLO-sA campaign-average Single Scattering Albedo (SSA) obtained by OSIRIS at 550 nm is 0.87. The strong absorption of the biomass burning plumes in the visible is consistent with the observations from the AERONET ground-based sun-photometers. The latter indicate a significant increase of the absorption at 440 nm, showing possible additional presence of absorbing organic species within the smoke plumes. Biomass burning aerosols are also vertically collocated with significant amounts of water content up to the top of the plume around 6 km height.

The average AAC Direct Radiative Effect (DRE) calculated from the airborne measurements in the visible range is +85 W m^{-2} (standard deviation of 26 W m^{-2}) with instantaneous values up to +200 W m^{-2} during intense events. Combination between water vapour and the strong positive aerosol forcing over the region explains possible feedbacks on cloud development. This new set of data represents a new opportunity to better constrain climate models and to study aerosol-cloud-radiation interactions over the South-East Atlantic region.

1. Introduction

Aerosols from natural and anthropogenic sources directly impact the climate by interacting with solar and telluric radiations and indirectly through interactions with cloud properties (IPCC, 2013). According to their origin and the atmospheric transport, aerosol particles are unequally distributed in the troposphere where they can reside for several days or weeks. As a consequence, their chemical, optical and microphysical properties also present a strong variability (Lagzi et al., 2014).

50   After gaseous carbon dioxide, Black Carbon (BC) aerosols are the strongest contributor to the global warming with comparable radiative forcing to methane. They are emitted through biofuel and fossil fuel combustion as well as biomass burning, accounting for about 60% and 40% of the total BC emissions, respectively (Ramanathan and Carmichael 2008). Biomass burnings also contribute to the additional emission of significant amount of water vapour, organic carbon and sulphates. In the South-eastern Atlantic region, smoke aerosol plumes can reach high altitudes (up to 6 km) and can be transported for several days in the atmosphere (Samset et al., 2014; Marenco et

55   al., 2016) and overlay low-level clouds which are persistent over water. BC particles significantly affect solar radiation and both cloud formation and properties (Kaufman and Fraser, 1997; Haywood et al., 2004), thereby producing significant direct and indirect radiative forcings (Keil and Haywood, 2003, Chand et al, 2009, De Graaf et al., 2019b). They also affect the satellite retrievals of cloud properties such as cloud droplet size and optical depth (Haywood et al., 2004).

60   However, such effects are still poorly quantified at global scale due to remaining uncertainties on Aerosol Above Clouds (AAC) loads and type (Waquet et al., 2013b). As a consequence, several studies have reported extremely high differences between modelled and observed aerosol radiative forcing as well between global climate models (Myhre et al. 2013; Samset et al., 2014). This is true especially in the South-eastern Atlantic region (Torres et al., 2012; Waquet et al., 2013; DeGraaf et al., 2014; Peers et al., 2016; Zuidema et al., 2016), where the horizontal and

65   vertical distributions of the biomass burning smoke in addition to its absorption properties have significant impacts on the direct radiative effect calculation. In the same region, Peers et al. (2016) reported disagreements between five AeroCom models and satellite observations of AAC from the Polarization and Directionality of Earth Reflectances (POLDER) instrument. These authors explained the differences in the models by the use of different parametrizations for the aerosol injection heights, vertical transport and absorption properties.

70   These considerations have motivated a significant number of intensive field campaigns between 1992 and 2018 (Formenti et al., 2019). As a matter of fact, the South-East Atlantic Ocean indeed represents a unique opportunity to study aerosol-cloud-radiation interactions and the absorption properties of biomass burning aerosols, which are still debated. Pistone et al. (2019) obtain Single Scattering Albedo (SSA) values for biomass burning aerosols from both airborne *in situ* and remote sensing methods during the Observations of Aerosols above Clouds and their

75   Interactions (ORACLES) airborne campaign performed close to the Namibian coast in August-September 2016. From a sweeping view mode imager (the Airborne Multi-angle SpectroPolarimeter Imager, AirMSPI), mean SSA values at 550 nm were observed between 0.83 and 0.89 in August-September 2016. Mean SSAs ranging between 0.82 and 0.92 (from June to October 2006) were also retrieved at 550 nm over a large region centred on the South-east Atlantic Ocean using POLDER (Peers et al., 2016). A previous study based on AERONET retrievals (Eck et

80   al., 2013) has shown similar SSA values during the fire season. The latter study demonstrated that the seasonal trend of SSA in this region was mainly due to a change on aerosol composition, and particularly on the black carbon fraction.

Because the simultaneous retrieval of aerosol and cloud properties is still challenging (Cochrane et al., 2019), the European Space Agency (ESA) and EUMETSAT developed a new spaceborne Multi-viewing, Multichannel,

85   Multi-polarization Imager (3MI) to be launched in 2022 on-board the METOP-SG satellite. To evaluate the next generation of retrieval algorithms, a 3MI airborne prototype, OSIRIS (Observing System Including PolaRisation in the Solar Infrared Spectrum; Auriol et al., 2008), has been developed at Laboratoire d'Optique Atmospheric (LOA, France). The total and polarized radiances sampled by OSIRIS between 440 and 2200 nm, and the new retrieval algorithms developed by Waquet et al. (2013) and Peers et al. (2015), allow to simultaneously retrieve

90   the aerosol and the cloud properties in case of aerosols above clouds. Additionally, polarimetric measurements constitute a promising opportunity for the simultaneous retrieval of the aerosol and the surface properties (Dubovik et al., 2011, 2019).

Therefore, the new observation capabilities proposed by the airborne instrument OSIRIS give an interesting opportunity to constrain climate models and satellite retrievals in a climate-sensitive region where high absorbing

95   aerosol load coexist with a stratocumulus cloud deck (Mallet et al., 2019).

In this paper we present the OSIRIS measurements of AAC collected during the AErosols, RadiatiOn and CLOuds in southern Africa (AEROCLO-sA) field campaign in Namibia during the biomass-burning period in 2017 (Formenti et al., 2019). The OSIRIS instrument was supplemented by the airborne sun-photometer PLASMA2 as well as the Lidar pour l'Etude des Interactions Aérosols Nuages Dynamique Rayonnement et du Cycle de l'Eau

100   (LEANDRE, Pelon et al., 1990) Nouvelle Génération (LNG, Bruneau et al., 2001). The present paper reports on optical and radiative properties of both aerosols and clouds retrieved during the AEROCLO-sA campaign close to

the Namibian coast, both over land and sea. Section 2 describes the flight trajectories and the main meteorological conditions encountered during the campaign. In Sect. 3, the OSIRIS, the airborne and ground-based sun-photometer and the airborne Lidar LNG retrieval methods are described. Section 3 reports the mean aerosol and cloud properties retrieved in the Namibian region. Finally, the results are summarised and discussed in Sect. 4.

2. Flights patterns and general atmospheric circulation description.

The AEROCLO-sA deployment comprised the measurements from the ground based station of Henties Bay, Namibia (22°6'S, 14°30'E; 20 m above sea level (a.s.l.)) from 23 August to 12 September 2017 (Formenti et al., 2019).

The airborne component was conducted by the SAFIRE Falcon 20 aircraft from 5 to 12 September 2017. Ten flights were performed over ocean and land in the area from 7°30'E to 20°E and from 17°S to 22°30'S (**Fig. 1**). Two pre-campaign flights (not presented here) were also performed over the Mediterranean Sea during the summer 2017. Those flights correspond to pristine conditions over both clear and cloudy ocean scenes and were used for instrumental calibration.

The locations of the OSIRIS observations used in the present study are shown in **Fig. 1a**. Several filters are applied to the OSIRIS measurements to ensure optimum conditions for the retrieval (i.e. homogeneous clouds fields and stable flight conditions), which slightly reduces the number of data (by 35%). As a first quality assurance, only stable flight conditions at high altitude (higher than 8 km a.s.l.) are selected. In addition, high altitude clouds and heterogeneous cloud scenes are rejected. In these conditions, a total of 2h15 of OSIRIS measurements were processed. **Figure 1b** also represents the PLASMA2 measurements used in the present study which corresponds to low flight levels and stable flight conditions.

Data from the Copernicus Atmospheric Monitoring System (CAMS) reanalysis (Flemming et al., 2017) allow to obtain the biomass burning plume trajectory at 6-hour resolution at a 0.75°x0.75° spatial resolution. In **Fig. 2**, the atmospheric circulation and the associated biomass burning plume during the field campaign are represented by the geopotential height and wind at 700 hPa and the biomass burning AOD at 550 nm. The plume path is displayed by highlighting the wind vectors at grid points with AOD higher than the 90th percentile of the AOD in the region (red arrows).

The regional atmospheric circulation on 8 September (**Fig. 2a**) represents the mean circulation during this period with air masses coming from tropical Africa, moving westward until Ascension Island which are then deflected to the South-East due to the anticyclone centred over southern Africa. These conditions were observed during most of the AEROCLO-sA campaign except on 5 September (**Fig. 2b**), when the anticyclone was centred over the Indian Ocean between the South African coast and Madagascar. During this specific day, air masses were mostly transported over the continent and dust emissions were reported from both the climate model and airborne the lidar measurements (Formenti et al., 2019).

3. Instrumentation

3.1 The 3MI airborne prototype: OSIRIS

The OSIRIS imager provides both total and polarized radiances measurements. The airborne instrument is characterized by two optical systems: one for the visible and near infrared range (VIS-NIR, from 440 to 940 nm) with a wild field-of-view of 114° and one for the shortwave infrared (SWIR, from 940 to 2200 nm) with a field-of-view of 105°. The 2D detectors, which are respectively a CCD matrix of 1392x1040 pixels and a mercury cadmium telluride (MCT) focal plane array of 320x256 pixels allow to obtain very high resolution images with a spatial resolution of 20 m for the VIS-NIR detector and around 60 m for the SWIR one at an height of 10 km. This high resolution allows to record the same scene up to 16 times (at 10 km height) from different viewing angles. Polarized measurements are available at 440, 490, 670, 870, 1020, 1600 and 2200 nm. Measurements without polarization capabilities are also performed in molecular absorption bands (763, 765, 910, 940, 1365 nm), and for a channel centred at 1240 nm, in addition to the channels previously listed.

The aerosol and cloud retrievals are performed using the OSIRIS measurements at 670 and 865 nm. A moving average is applied on measurements over few pixels before the retrieval is achieved. The related radiometric noise is then estimated to be lower than 5.10^{-4} and 5.10^{-3} for the total and polarized normalized radiances, respectively. After all radiometric and geometric treatments are applied to the data (Auriol et al., 2008), the errors due to absolute

Atmospheric
Chemistry
and Physics
Discussions

calibration are expected to be lower than 3% for these channels. The absolute calibration accuracy was improved for the visible radiances using in-flight calibration technics (Hagolle et al., 1999) applied to OSIRIS measurements acquired over the Mediterranean Sea.

155 The algorithm used to retrieve the AAC properties with OSIRIS is based on an Optimal Estimation Method (OEM) developed for the POLDER instrument (Waquet et al., 2013). This method allows to simultaneously retrieve the aerosol and the cloud properties (Waquet et al., 2013 and Peers et al., 2015). Here, the aerosol retrieval is performed using the measurements in the solar plane of each image. The aerosol properties are then assumed to be spatially homogenous over the entire OSIRIS visible image (of about 20×20 km^2). Finally, the cloud properties
160 are retrieved pixel by pixel over the entire image. As demonstrated in Waquet et al. (2013), this procedure increases the sensitivity of the algorithm to the aerosol properties.

The algorithm mainly provides AOD, SSA, extinction Angström exponent (α) and the Cloud Optical Thickness (COT). SSA is defined as the ratio of the scattering to the extinction coefficient and primarily depends on the aerosol absorption (i.e. the imaginary part of the complex refractive index) and also the particles size (Dubovik et
165 al.,1998 ; Redemann et al., 2001). The Angström exponent is indicative of the particles size (Reid et al., 1999; Schuster et al., 2006). The retrieved quantities are used to compute the instantaneous DRE over the solar spectrum, considering two main assumptions on the aerosol microphysics: (1) the complex refractive index of aerosols is assumed spectrally invariant; the imaginary part is retrieved and the real part value is fixed to 1.51, which is a reasonable average value for biomass burning aerosols (Dubovik et al., 2000) and (2) the particles size is retrieved
170 only for the fine mode (particle diameters below 1 µm). The main source of uncertainties on the OSIRIS aerosol retrievals is the assumption made for the real refractive index (Waquet et al., 2013a). The calculations were perturbed with different values of the real refractive index (1.51 ± 0.04) and additional error terms were added to the retrieval errors provided by the OEM (Waquet et al., 2013). Moreover, the polarized measurements acquired for scattering angles larger than 130° are sensitive to the 3D cloud geometry effects on radiative transfer (Cornet
175 et al., 2018). Since clouds are assumed to be plane parallel in the simulations, the method is simply applied to observations acquired for scattering angles smaller than 130°.

Figure 3 shows an example of the measured and modelled radiances after the convergence is reached. It shows that the method allows to robustly model the selected data within the measurements noise. For these values of scattering angles, the sensitivity of polarization to cloud microphysics is minimized and the cloud droplet effective
180 radius is assumed to be equal to 10 microns, which is the mean value for the stratocumulus clouds observed over the domain of interest (Deaconu et al., 2019).

3.2 The airborne Sun-photometer: PLASMA 2

PLASMA 2 (Photomètre Léger Aéroporté pour la surveillance des Masses d'Air version 2, Karol et al., 2013) is an airborne Sun-tracking photometer (referred as #950 on AERONET) which was on-board the SAFIRE Falcon
185 20 during the AEROCLO-sA campaign. The AOD of the atmospheric column above the aircraft is retrieved at nine wavelengths (340, 379, 440, 500, 532, 674, 871, 1020 and 1641 nm) from the PLASMA2 measurements. PLASMA (versions 1 and 2) observations have been validated against *in situ*, AERONET and satellite measurements (Mallet et al., 2016; Rivellini et al., 2017; Torres et al., 2017; Formenti et al., 2018; Hu et al., 2018), indicating that the accuracy on the AOD retrievals is of the order of 0.01 regardless of the wavelength. During
190 AEROCLO-sA, several low-level flights were performed, typically in overcoast conditions over the ocean to retrieve the AAC optical properties and in clear sky conditions over land. The fraction of fine and coarse mode AOD is derived from the large spectral range of PLASMA2 using the GRASP algorithm (Dubovik et al., 2014, Torres et al., 2017). GRASP also allows to retrieve the volume size distribution using an assumed complex refractive index (i.e. 1.50+0.025) and assuming a bimodal lognormal particles size distribution with fixed modal
195 widths.

3.3 Airborne lidar LNG

The vertical structure of the aerosol and cloud layers below the aircraft was obtained from the nadir-pointing airborne lidar LNG. The signal backscattered to the LNG system telescope at 1064 nm is range-square-corrected to produce atmospheric reflectivity. Total attenuated backscatter coefficient (ABC) profiles are derived from
200 atmospheric reflectivity profiles by normalizing the atmospheric reflectivity above the aerosol layers to the molecular backscatter coefficient profiles. Hence the slope of the lidar reflectivity above 6.5 km a.s.l. matched that of the molecular backscatter derived from dropsonde measurements of pressure and temperature. The vertical resolution of the ABC profiles is 30 m and profiles are averaged over 5 s, yielding a horizontal resolution of 1 km

205 for an aircraft flying at 200 m s^{-1} on average. It is worth noting that ABC as observed with LNG is sensitive to both aerosol concentration and aerosol hygroscopicity. Indeed, relative humidity in excess of 60% modify the size and the complex refractive index of aerosol, and hence their optical properties, enhancing the ABC (e.g. Randriamiarisoa et al., 2006).

3.4 Ground-based AERONET sun-photometer measurements.

210 To put the aircraft observations into context, we analysed observations form 15 August to 15 September 2017 from the 15 AERONET stations located in the South-eastern Atlantic region. The full column integrated properties (i.e. AOD, complex refractive index, extinction Angström exponent, SSA and AOD fine mode fraction) have been averaged for each site and are shown in **Fig. 4.** Four AERONET stations are located in the AEROCLO-sA flight domain: Windpoort, Henties Bay, Gobabeb, as well as HESS, located in the southern part of the domain, 200 km south-East of Henties Bay, and outside of the flight tracks. During the campaign, and due to the persistent cloud

215 cover, the measurements available at Henties Bay and Gobabeb were sparse. Therefore, the Windpoort station, located at 250 km from the Namibian Coast, is a more suitable station to monitor the aerosol evolution during the campaign. Additional interesting comparison data are provided by the Namibe station, located in the northern part of the AEROCLO-sA region, and more influenced by biomass burning emissions from central Africa than the Windpoort site (therefore exhibiting higher AODs). Outside the AEROCLO-sA domain, and as shown by the

220 atmospheric circulation patterns in **Fig. 2**, biomass burning plumes were often transported towards Ascension Island. This remote location (i.e. 3000 km offshore the Angola coast) gives an opportunity to study the evolution of the biomass burning aerosols during their transport and aging (Zuidema et al., 2016; Mallet et al., 2019).

4. Results
4.1 Aerosol extinction optical thickness.

225 **Figure 5** reports the AERONET AODs measured at the Namibe, Windpoort, Ascension Island and Sao Tome sites during the biomass burning period (from 15 August to 15 September 2017). A moderate aerosol loading is observed at the Sao Tome and Namibe sites at the beginning of the selected period with mean AOD of 0.76 and 0.48 at 550 nm, respectively, whereas the Windpoort and Ascencion Island sites record mean AOD of 0.10 and 0.19 at 550 nm, respectively. A first increase of the aerosol loading is observed between 27 August and 1

230 September 2017 at the Namibe and Windpoort sites (AOD up to 0.88 and 0.73 at 550 nm, respectively), a second increase between 3 and 8 September at the Namibe, Windpoort and Sao Tome sites (AOD up to 1.80, 1.54 and 1.72 at 550 nm, respectively), and a third increase starting on 13 September at the Namibe and Windpoort sites (AOD up to 1.45 and 0.84 at 550 nm, respectively). During the AEROCLO-sA flight period, the strongest aerosol loadings in the AEROCLO-sA region were observed on 5 September and the lowest on 12 September. This

235 variation of the aerosol loading is mainly explained by the changes in the atmospheric circulation as demonstrated in Sect. 2.

The Aerosol Backscatter Coefficient (ABC) at 1064 nm on 12 September 2017 obtained from the airborne Lidar is shown **Fig. 6a**. The aerosol signal is mainly concentrated between the stratocumulus top at around 1 km and 6 km height. This vertical distribution well represents the general condition during the AEROCLO-sA campaign

240 (Chazette et al., 2019). For this same day, **Fig. 6b** shows the spectral AOD measured by OSIRIS, PLASMA2 and the ground-based Windpoort and Namibe AERONET stations. The OSIRIS above-cloud retrievals were performed using measurements at an altitude of about 9 km a.s.l., corresponding to the top of the descent in loop. Contrary to the configuration of OSIRIS on the SAFIRE Falcon 20 aircraft, PLASMA2 is an upward looking instrument. Therefore, the above-cloud aerosol properties from PLASMA2 were obtained from the measurements

245 at the bottom of the descent in loop, above the cloud top. AOD retrieved from OSIRIS and PLASMA2 measurements agree within ± 10% at 670 nm (**Fig. 6b**, **Table 1**), and are in between the measurements of the two AERONET stations. Bias between PLASMA2 and AERONET AODs are around 70% for every wavelengths, whereas OSIRIS measurements agree with AERONET AODs from 20% with Windpoort measurements at 870 nm to 67% with Namibe measurements at 670 nm.

250 **Table 1** shows this same comparison from four loops, showing a very good agreement between OSIRIS and PLASMA2 for variable AOD conditions (from 0.36 and 0.74 at 670 nm). This indicates that the OSIRIS above-cloud AOD retrieval is robust independently on the aerosol loading. Note that, on 5 September, the aircraft did not reach the cloud top level at the end of the loop, which causes a higher bias (30%) between the AOD from PLASMA2 and OSIRIS's.

Atmospheric
Chemistry
and Physics

Discussions

255   **Figure 7a** shows a time series of the OSIRIS above-cloud AOD at 490, 670 and 870 nm on 12 September 2017. The 40-minute slot represents a transect of about 400 km along the coast-line (in yellow **Fig. 1a**) with a north cape. A slight variability is observed on the AOD with a south-north gradient. 30 minutes after the segment at high altitude, the collocated observations from PLASMA2 at low altitude are consistent with OSIRIS, with the AOD from PLASMA2 being larger by 10% than OSIRIS. Parallel measurements of the airborne lidar LNG demonstrate
260   the small spatial variability observed on 12 September with homogeneous distribution of aerosols in the troposphere with low aerosol signal (ABC below 1.10^{-6} m^{-1} sr^{-1}).

Figures 7b shows a histogram of the above-cloud AOD from OSIRIS at 550 nm for each flight of the campaign. The retrieved AODs are ranging from 0.2 to 1.2. The median AOD depends on the flight with a maximum of 0.87 on 5 September and a minimum of 0.35 on 12 September. The 7, 8 and 9 September have a median AOD values
265   of 0.73, 0.82 and 0.62, respectively. These high AODs are consistent with the large value typically observed close to the coast by satellites (0.6 at 550 nm, Peers et al., 2016) and aircraft polarimeter measurements in the South-eastern Atlantic (around 0.75 at 550 nm, Pistone et al., 2019).

4.2 Angström exponent and particle size distribution

Figure 8a describes the volume particle size distributions retrieved from PLASMA2 measurements at different
270   altitudes during the descent in loop on 7 September 2017. The AERONET particle size retrievals from the Windpoort station are also shown. The size distribution is generally characterised by a dominant fine mode between 500 m and 5000 m. This is consistent with the dominant fine mode typically observed in previous studies at an altitude of 1 to 6 km in this region (Toledano et al., 2007; Russell et al., 2010; Kumar et al., 2013). Measurements show a rather constant fine-coarse mode ratios within the aerosol plume. For the descent in loop
275   over cloud on 7 September 2017, fine mode particles contributed to 97 % of the total AOD at 670 nm between 1000 m and 4000 m. The mean Angström exponent value obtained from PLASMA2 measurements is about 1.9 with an accuracy of 0.1. According to AERONET measurements, during the campaign period, the amount of coarse mode particles is also extremely weak and does not exceed 5% of the columnar AOD (**Fig. 4**). The smallest particles (Angström exponent larger than 2) are generally observed in the northern part of the Namibian region
280   (**Fig. 4**).

Figures 8 b, c and d show the altitude, the AOD and the extinction Angström exponent measured by PLASMA2 for straight levelled runs below 2000 m a.s.l.. The second flight on 12 September, over the Etosha Pan (black line) presents a strong AOD gradient between 0.30 and 0.82, and a strong Angström exponent gradient between 1.55 and 2.27, not correlated to altitude variations. During this specific flight, the measurements over the Etosha Pan
285   were performed at around 1300 m a.s.l.. The Etosha Pan is the main source of dust emission in this region and it is characterised by an extremely dry surface at this time of year. In these conditions, the particles size distribution retrieved by PLASMA2 over the South-western part of the flight, over the Etosha Pan, is characterized by a significant additional contribution of coarse mode particles ($\alpha_{440-870}$ = 1.55). Toward the North-Eastern part of the flight, the aerosol properties retrieved by PLASMA2 are less influenced by the dust emissions from the pan, and
290   are more representative of the properties of fine mode particles from biomass burning ($\alpha_{440-870}$ = 2.27).

The values of Angström exponents retrieved above clouds from OSIRIS and PLASMA2 are around 2.0 ± 0.2. In agreement with the PLASMA2 analysis, the $\alpha_{490-870}$ histogram shown in **Fig. 8e** indicates different aerosol types. The maximum $\alpha_{490-870}$ is observed on 12 September (median of 2.15), and the minimum on 8 September (median of 1.75). $\alpha_{490-870}$ values are generally constant for every flight, as in the case on 12 September (**Fig. 7a**). The lowest
295     $\alpha_{490-870}$ values, around 1.7, are found less than 50 km away from the Namibian coast and were observed during the flight on 8 September. This behaviour might be explained by the influence of dust particles generated on the continent with higher coarse mode particle fraction. The hygroscopic growth of biomass-burning particles potentially occuring during their transport over the ocean might also explain the differences observed in the aerosol optical properties from one flight to another. The aerosols observed on 5 September were directly transported from
300   Central Africa without a long transport over the Atlantic Ocean (**Fig. 2b**). This specific circulation might explain the higher $\alpha_{490-870}$ (mean of 1.91) observed above clouds during this flight, which indicates smaller particles than the ones observed for instance on 8 September. These changes in the fine mode size are also suggested from the analysis of the volume fine mode properties obtained from PLASMA2 inversions. Lower values of the volume mean radius of the fine mode particles are retrieved on 5 and 12 September (r_v = 0.18 and 0.15 µm, respectively)
305   rather than on 8 September (r_v = 0.20 µm).

AERONET Ångström exponents are around 5 % lower than PLASMA2 measurements and from 8 to 25 % lower than OSIRIS inversions (**Table 1**). The bias between AERONET and OSIRIS Ångström exponents can mainly be explained by the presence of coarse mode particles that are not explicitly taken into account in the POLDER algorithm when biomass burning layers are detected above clouds (Waquet et al., 2013a). This is particularly

310 observed for the flight on 12 September due to a slightly less dominant fine mode compared to other flights (i.e. mean fine mode fraction of 90% on 12 September instead of 95% on average for the field campaign). This neglected coarse mode could also explain why OSIRIS slightly underestimated AOD compared to PLASMA 2 on 12 September (**Fig. 7a**).

4.3 Complex refractive index and single scattering albedo

315 The analysis of AERONET measurements over the biomass-burning period also provides us with a spatial distributed view of the aerosol complex refractive index and single scattering albedo. Values of SSA at 675 nm (hereafter SSA_{675}) are generally spatially homogeneous over land with a mean value of 0.85 (25th and 75th percentiles of 0.84 and 0.86, respectively). The highest SSA_{675} is observed at the Namibe station (**Fig. 4**) with a mean value of 0.87, while the lowest values are observed at the Bonanza and Mongu Inn stations (mean SSA_{675} of

320 0.82). In correspondence, a mean refractive index of $1.51 + 0.027i$ at 675 nm is retrieved. The real part of the refractive index at 675 nm ranges from 1.41 at Henties Bay to 1.54 at Bonanza, and the imaginary part at 675 nm ranges from 0.008 at Henties Bay to 0.032 at Bonanza. The known environmental characteristics of Henties Bay, a coastal site with high content of sea salt and sulphate aerosols, frequent fog and a persistent as well as elevated relative humidity (Formenti et al., 2019; Klopper et al., 2020), support the low values of the real and imaginary

325 refractive indices. **Figure 4** also shows different behaviours on the spectral variation of the imaginary part of the refractive index k in the South-Eastern region. k_{441} is higher than k_{675} (up to 43%) on the northern part of the region, and lower (up to 10%) on the southern part of the region. The largest ratio between k_{441} and k_{675} is observed at the Namibe station with k_{441} higher than k_{675} by more than 40%.

The SSA of AAC can also be observed from OSIRIS inversions for the entire AEROCLO-sA flight campaign.

330 **Figure 9a** shows the SSA histograms of each analysed AEROCLO-sA flight. Results show absorbing property in this region with a mean SSA of 0.87 at 550 nm for the full campaign (range 0.75-0.95). Average values of above-cloud SSA are similar amongst flights (0.87 on 9 September and 0.89 on 5 September). Knowing that the atmospheric circulation regimes were different on those days, this suggests that competing effects (emission regimes and types, ageing processes, …) could occur.

335 **Figure 9b** compares the spectral variation of the SSA from OSIRIS during the full campaign to various complementary measurements: the concurrent ground-based AERONET at the Windpoort and Namibe sites, the retrievals of the airborne imager AirMSPI during ORACLES-2016 (Pistone et al., 2019), and the mean POLDER retrievals above cloud for the South-eastern region from 2005 to 2009 during the fire season (Peers et al., 2016). The SSA from OSIRIS are less than 1% different from the ORACLES-2016 AirMSPI observations. Both

340 measurements are consistent with the multi-year average SSA from POLDER during the biomass burning period (less than 2% difference), as expected as these estimates are all based on polarimetric measurements. A higher bias (about 3%) compared to OSIRIS inversion is observed with AERONET retrievals at Windpoort, where the SSA is lower irrespectively of the wavelength. On the other hand, the measurements at the Namibe AERONET station are consistent with our retrievals at 670 nm, but not at 440 nm, where the SSA is significantly lower. This

345 trend does not appear in the ORACLES measurements from AirMSPI, which were performed farther from the coasts over the ocean. According to Kirchstetter et al. (2004), a decrease of the SSA at 440 nm can be partly explained by the presence of light-absorbing organic carbon (brown carbon). Unlike at the Namibe site, the SSA at Windpoort, located farther from the fire sources, was generally found to decrease from 440 to 875 nm.

4.4 Integrated water content

350 The integrated water vapour can be derived from extinction measurements at 940 nm (Halthore et al., 1997). In **Fig. 10**, one can note the linear relationship between the water vapour content and the AOD at 550 nm from PLASMA2, especially for the higher range of water vapour concentration. The highest column concentrations of water vapour (up to 2.4 g cm^{-2}) are observed for the two flights of 8 September. This correlation could be explained by the meteorological conditions, which would be responsible for the simultaneous transport of aerosols and water

355 vapour (Adebiyi et al., 2015, Deaconu et al., 2019), or by the wood moisture emitted in tropical area, biomass burning can also generate water vapour (Betts and Silva Dias, 2010; Sena et al., 2013). The variability observed in the relationship between AOD and water vapour through PLASMA2 measurements could also be the result of

different emission regimes observed during the various flights. On the opposite, no correlation is observed for the second flight of 12 September with lower water vapour content (below 1 g cm^{-2}). This particularity could be explained by the in-land location of the measurements performed above the Etosha Pan associated with dryer air masses.

4.5 Cloud properties

The OSIRIS measurements also provide us with the optical properties of clouds with a high spatial resolution. For each pixel of the OSIRIS CCD matrix, the Cloud Optical Thickness (COT) can be retrieved at a spatial resolution reaching 20 m for a flight altitude around 10 000 m a.s.l.. **Figure 11a** shows a retrieved field of COT on 7 September at 09:37 UTC at the top of the first ascent of the flight close to the coast. COT values at 550 nm range from 5 to 30 with a mean value of 16.

To analyse the full AEROCLO-sA dataset, we chose to select the central pixel of every OSIRIS CCD matrix. This selection allows us to get rid of the scene details of each OSIRIS measurements and is well representative of the COT distribution in the region. As all the flights were performed between 8:00 and 11:00 local time, measurements refer to similar atmospheric thermodynamics and sun conditions. **Figure 11b** shows the distribution of COT values at 550 nm for the whole campaign. The COT at 550 nm ranges from 5 to 35. On 5 and 8 September, a mean COT of 11 ± 4 is obtained while the mean COT is 15 ± 4 on 9 September and 19 ± 6 on 7 and 12 September. Mean values are similar for each flight but particularly high values are observed on 7 and 12 September. As shown in **Fig. 11c**, COT can be related to the distance from the coastline. An increase from 10 to 30 is observed from the Namibian coast up to 100 km off the coast. On 7 September, measurements were performed up to 350 km away from the coastline. For this flight, a maximum value of COT is observed around 100 km away from the coast and then, the COT decreases down to 10 at around 250 km. It was noted, during the field campaign, that the clouds were generally optically less thick in the vicinity of the Namibian coast and more difficult to forecast.

4.6 Direct radiative effect

The Direct Radiative Effect (DRE) calculations are performed over the solar spectrum (0.2-4 microns) with the radiative transfer code GAME (Dubuisson et al., 1996). We follow the procedure described in Peers et al. (2015), with the only differences that the DRE calculations are performed online and are based on OSIRIS retrievals in the visible and near-infrared ranges. Considering the time period and location, a tropical model was assumed for the vertical atmospheric profile (McClatchey, 1972).

The distribution of the observation-based, instantaneous and one-dimensional AAC DRE in the solar spectrum from OSIRIS measurements is shown in **Fig. 12** for every flight during AEROCLO-sA. Calculations show positive DRE in agreement with above-cloud observations from Zhang et al. (2016) in regions influenced by biomass burning emissions. Keil and Haywood (2003) also estimated a mean value of above-cloud DRE of +11.5 W m^{-2} above cloud and of – 13 W m^{-2} in clear sky conditions (mean SSA of 0.90 at 550 nm).

The above-cloud instantaneous DRE obtained from OSIRIS measurements ranges from + 10 to + 200 W m^{-2} with mean values between + 61 W m^{-2} on 12 September and +105 W m^{-2} on 7 September. The mean DRE for the full campaign is +85 W m^{-2}. De Graaf et al. (2019b) compared the observations from SCIAMACHY (Scanning Imaging Absorption Spectrometer for Atmospheric Chartography, Bovensmann et al., 1999), POLDER (Peers et al., 2015) and OMI-MODIS (De Graaf et al., 2019a) satellite retrievals in the South Atlantic region. For the larger area (10°N-20°S, 10°W-20°E), these authors reported that the average August 2006 DRE was +39.5, +34.5 and +47 W m^{-2}, respectively. Meyer et al. (2015) also reported DRE through multi-spectral measurements of MODIS in the region. Their work highlights the significant effects of the assumed aerosol model in radiative retrieval by up to +10 W m^{-2} in the region. Hence, the DRE retrievals are mainly affected by the absorption property of the assumed aerosol model (Zhang et al., 2016). The larger DRE retrieved during AEROCLO-sA is thus correlated to strong absorption properties, to high aerosol loading and to high cloud albedo observed during this period.

5. Conclusion

A new set of data of cloud and above-cloud aerosol properties was acquired during the AEROCLO-sA campaign over Namibia during the biomass-burning period of 2017 by the OSIRIS radiometer deployed during ten scientific flights from 5 to 12 September 2017. Five flights are selected for OSIRIS analyses presenting stable cloud conditions. Aerosol and cloud properties at a 20-meter resolution with well-quantified uncertainties are retrieved by radiometric inversion.

410 Measurements were performed in an extreme environment with high loading of biomass burning particles transported above a semi-permanent stratocumulus cloud deck. The high aerosol load (above-cloud AOD around 0.7 at 550 nm) retrieved from OSIRIS measurements matches the direct AOD measurements of the airborne Sun-photometer PLASMA2 within 10%, which contribute to validate the application of aerosol above cloud algorithms on airborne polarimeter. Biomass burning aerosol layers are mainly composed of fine mode particles, with Angström exponents varying between 1.6 and 2.2, depending on the plume history and intrinsic properties.

415 Ground-based AERONET measurements on the continent generally show slightly lower values of Angström exponent (close to 1.7 on average), which is likely due to the presence of additional coarse particles located in the boundary layer. Another reason which could explain differences on Angström exponent values is the hygroscopic effects influencing particle size.

Biomass burning aerosols transported over the South-eastern Atlantic Ocean represent a high absorbing effect which significantly impacts the climate. Mean above-cloud SSA of 0.87 at 550 nm were obtained from OSIRIS

420 measurements. Rather constant aerosol absorbing properties were observed in the Namibian region during the campaign in the visible range of OSIRIS. This effect can be due to competition between different effects as the general atmospheric circulation, the emission index and ageing processes. AERONET retrievals indicate an increase of the aerosol absorption at 440 nm over some specific sites, which suggests a modification of the plume composition, in particular regarding the ratio between the light-absorbing organic (brown) and soot (black) carbon.

425 Brown carbon should thus be considered for the modelling of the absorption properties of the smoke plumes observed closer to the fire regions. Additional measurements acquired in the UV band by the airborne micro-polarimeter Ultra-Violet (MICROPOL), also operated on the Safire Falcon-20 during AEROCLO-sA, will be included in the OSIRIS algorithm to further investigate this possibility.

A significant part of climate uncertainty in the South-eastern Atlantic region is also explained by the lack of

430 measurement of stratocumulus cloud properties. The characteristics of the airborne imager OSIRIS give the opportunity to retrieve cloud properties with a high spatial resolution. During the AEROCLO-sA campaign, a mean COT of 10 at 550 nm was observed. Measurements up to 350 km off the coastline allow us to probe stratocumulus property in different conditions. Results showed a maximum COT of 30 reached at 100 km off the coastline. The polarized measurements acquired by OSIRIS at 1620 and 2200 nm could be included in the retrieval

435 in order to further characterise the cloud microphysics under different conditions in the region.

As a result of the elevated above-cloud AODs, the strong absorption by aerosols, and the high cloud albedo, significant positive instantaneous aerosol direct radiative effects in the solar spectrum were observed close to the Namibian coast. The mean AEROCLO-sA instantaneous DRE value is +85 W m^{-2} for AAC. Our observations are in agreement with previous studies indicating a strong positive aerosol forcing over the region (De Graaf et al.,

440 2019b, 2020) with possible feedbacks on cloud development due to both aerosol and water vapour combined radiative effects (Deaconu et al., 2019). However, the aerosol DRE on the AEROCLO-sA region is higher than the mean DRE observed in the southern Atlantic region, mainly because of the exceptional atmospheric conditions sampled during the flights (high loads of absorbing aerosols and high cloud albedo). As demonstrated by Cochrane et al. (2019) based on the ORACLES campaigns in 2016 and 2017, the DRE also strongly depends on the cloud

445 scene, in particular on the cloud albedo. Field campaigns in the southern Atlantic region between 2016 and 2018 have shown a high variability of the cloud albedo due to the heterogeneity of the cloud fraction, the cloud droplet size and the cloud optical thickness. Spatial resolution used by observations also have significant impacts on the retrievals of cloud properties and consequently on radiative properties (De Graaf et al., 2019a).

In conclusion, the airborne multi-viewing, multi-channel, multi-polarisation measurements in the region allow us

450 to improve the definition of above-cloud aerosol properties in the region and estimate climate response to the presence of high absorption particles above cloud. Mean aerosol and cloud properties established from airborne remote sensing measurements during the AEROCLO-sA campaign are valuable to constrain climate models and satellite retrievals of the aerosol-cloud-climate interactions in this region.

Nonetheless, many unresolved questions remain on the transport and ageing of biomass burning particles in the

455 region. A synergistic analysis of multi-campaign data will benefit this analysis. The high spatial resolutions, offered by the airborne polarimeter OSIRIS and Lidar LNG data acquired during the AEROCLO-sA campaign, also offer the opportunity to improve retrievals of the heating rate profiles, based on the satellite method described in Deaconu et al (2017). These retrievals would benefit from the aerosol-cloud interactions studies in the South-eastern Atlantic region.

460 **Acknowledgements**

Atmospheric
Chemistry
and Physics
Discussions

Author contributions

AC performed simulations, analyses of airborne and AERONET data, and write the manuscript under the
supervision of FW. PF, FW, CF, and MM, designed the original AEROCLO-sA observational concept, and co-
480 led the 5-year investigation. FA, LB, CD, RL, and JMN developed, calibrated and assured high quality
measurements of the OSIRIS instrument during the campaign. LB assured PLASMA2 calibration, settings and
data processing. CD assured PLASMA2 measurements during the campaign. FW and FPe developed POLDER
algorithms. PG and FPa co-led the development of the OSIRIS and PLASMA2 instruments. OD and BT developed
and allow access of the GRASP algorithm. MG established CAMS simulations. CF provided LNG extinction
485 profiles. Every co-authors contributed to the scientific analysis and to the writing of the manuscript.

Competing interests

PF is guest editor for the ACP Special Issue "New observations and related modelling studies of the aerosol–
cloud–climate system in the Southeast Atlantic and southern Africa regions". The remaining authors declare that
they have no conflicts of interests.

490 **Data availability**

We thank the AERONET PIs Brent Holben, Jens Redemann, Carlos Ribeiro, Nichola Knox, Stuart Piketh, and
their staff for establishing and maintaining the AERONET sites used in this investigation.

The AEROCLO-sA data are available in the BAOBAB platform available on https://baobab.sedoo.fr/AEROCLO/
and maintained by the French national data center Data Terra/AERIS. In particular, the dataset used in this paper
495 are: OSIRIS (https://doi.org/10.6096/AEROCLO.1802), LNG (https://doi.org/10.6096/AEROCLO.1774), and
PLASMA2 (https://doi.org/10.6096/AEROCLO.1807).

CAMS simulations were realized by MG. Biomass burning aerosol AODs are available at
https://baobab.sedoo.fr/Data-Search/?datsId=1782&project_name=AEROCLO.

Above cloud POLDER data are available from the ICARE website.

500 **References:**

Adebiyi, A. A., Zuidema, P., and Abel, S. J.: The convolution of dynamics and moisture with the presence of
shortwave absorbingaerosols over the southeast Atlantic, J. Climate, 28, 1997–2024,https://doi.org/10.1175/JCLI-
D-14-00352.1, 2015.

Auriol, F., Léon, J.-F., Balois, J.-Y., Verwaerde, C., François, P., Riedi, J., Parol, F., Waquet, F., Tanré, D. and
505 Goloub, P.: Multidirectional visible and shortwave infrared polarimeter for atmospheric aerosol and cloud
observation: OSIRIS (Observing System Including PolaRisation in the Solar Infrared Spectrum), in Multispectral,
Hyperspectral, and Ultraspectral Remote Sensing Technology, Techniques, and Applications II, vol. 7149, p.
71491D, International Society for Optics and Photonics., 2008.
Betts, A. K. and Silva Dias, M. A. F.: Progress in understanding land-surface-atmosphere coupling from LBA
510 research, J. Advances in Modeling Earth Systems, 2(2), 2010.

Bovensmann, H., Burrows, J. P., Buchwitz, M., Frerick, J., Noël, S., Rozanov, V. V., Chance, K. V. and Goede,
A. P. H.: SCIAMACHY: Mission objectives and measurement modes, J. Atmos. Sci., 56(2), 127–150, 1999.

Atmospheric
Chemistry
and Physics
Discussions

Bruneau, D., Quaglia, P., Flamant, C., Meissonnier, M. and Pelon, J.: Airborne lidar LEANDRE II for water-vapor profiling in the troposphere. I. System description, Applied optics, 40(21), 3450–3461, 2001.

515   Chand, D., Wood, R., Anderson, T. L., Satheesh, S. K. and Charlson, R. J.: Satellite-derived direct radiative effect of aerosols dependent on cloud cover, Nature Geoscience, 2(3), 181–184, doi:10.1038/ngeo437, 2009.

Chazette, P., Flamant, C., Totems, J., Gaetani, M., Smith, G., Baron, A., Landsheere, X., Desboeufs, K., Doussin, J.-F. and Formenti, P.: Evidence of the complexity of aerosol transport in the lower troposphere on the Namibian coast during AEROCLO-sA, Atmos. Chem. Phys., European Geosciences Union, 2019, 19,pp.14979-15005.
520   10.5194/acp-19-14979-2019, 2019.

Cochrane, S. P., Schmidt, K. S., Chen, H., Pilewskie, P., Kittelman, S., Redemann, J., LeBlanc, S., Pistone, K., Kacenelenbogen, M., Segal Rozenhaimer, M., Shinozuka, Y., Flynn, C., Platnick, S., Meyer, K., Ferrare, R., Burton, S., Hostetler, C., Howell, S., Dobracki, A. and Doherty, S.: Above-Cloud Aerosol Radiative Effects based on ORACLES 2016 and ORACLES 2017 Aircraft Experiments, Atmos. Meas. Tech. Discuss., 2019, 1–50,
525   doi:10.5194/amt-2019-125, 2019.

Cornet, C., Laurent, C., Waquet, F., Szczap, F., Deaconu, L., Parol, F., Vanbauce, C., Thieuleux, F. and Riédi, J.: Cloud heterogeneity on cloud and aerosol above cloud properties retrieved from simulated total and polarized reflectances, Atmos. Meas. Tech., European Geosciences Union, 2018, 11 (6),pp.3627-3643. 10.5194/amt-11-3627-2018, 2018.

530   Deaconu, L., Waquet, F., Josset, D., Ferlay, N., Peers, F., Thieuleux, F., Ducos, F., Pascal, N., Tanré, D. and Pelon, J.: Consistency of aerosols above clouds characterization from A-Train active and passive measurements, Atmos. Meas. Tech., 10(9), 3499–3523, 2017.

Deaconu, L. T., Ferlay, N., Waquet, F., Peers, F., Thieuleux, F. and Goloub, P.: Satellite inference of water vapor and aerosol-above-cloud combined effect on radiative budget and cloud top processes in the Southeast Atlantic
535   Ocean, Atmos. Chem. Phys. Discuss., 2019, 1–34, doi:10.5194/acp-2019-189, 2019.

Dubovik, O., Holben, B. N., Kaufman, Y. J., Yamasoe, M., Smirnov, A., Tanré, D. and Slutsker, I.: Single-scattering albedo of smoke retrieved from the sky radiance and solar transmittance measured from ground, J. Geophys. Res., 103(D24), 31903–31923, doi:10.1029/98JD02276, 1998.

Dubovik, O., Smirnov, A., Holben, B. N., King, M. D., Kaufman, Y. J., Eck, T. F. and Slutsker, I.: Accuracy
540   assessments of aerosol optical properties retrieved from Aerosol Robotic Network (AERONET) Sun and sky radiance measurements, J. Geophys. Res., 105(D8), 9791–9806, doi:10.1029/2000JD900040, 2000.

Dubovik, O., Herman, M., Holdak, A., Lapyonok, T., Tanré, D., Deuzé, J. L., Ducos, F., Sinyuk, A. and Lopatin. A.: Statistically optimized inversion algorithm for enhanced retrieval of aerosol properties from spectral multi-angle polarimetric satellite observations, Atmos. Meas. Tech., 4(5), 975–1018, doi:10.5194/amt-4-975-2011,
545   2011.

Dubovik, O., Lapyonok, T., Litvinov, P., Herman, M., Fuertes, D., Ducos, F., Torres, B., Derimian, Y., Huang, X., Lopatin, A., Chaikovsky, A., Aspetsberger, M. and Federspiel, C.: GRASP: a versatile algorithm for characterizing the atmosphere, SPIE Newsroom, doi:10.1117/2.1201408.005558, 2014.

Dubovik, O., Li, Z., Mishchenko, M. I., Tanré, D., Karol, Y., Bojkov, B., Cairns, B., Diner, D. J., Espinosa, W. R.
550   and Goloub, P.: Polarimetric remote sensing of atmospheric aerosols: Instruments, methodologies, results, and perspectives, J. Quant. Spectroscopy Rad. Transfer, 224, 474–511, 2019.

Dubuisson, P., Buriez, J. C. and Fouquart, Y.: High spectral resolution solar radiative transfer in absorbing and scattering media: Application to the satellite simulation, J. Quant. Spectroscopy Rad. Transfer, 55(1), 103–126, 1996.

555   Eck, T. F., Holben, B. N., Reid, J. S., Mukelabai, M. M., Piketh, S. J., Torres, O., Jethva, H. T., Hyer, E. J., Ward, D. E., Dubovik, O., Sinyuk, A., Schafer, J. S., Giles, D. M., Sorokin, M., Smirnov, A. and Slutsker, I.: A seasonal trend of single scattering albedo in southern African biomass-burning particles: Implications for satellite products and estimates of emissions for the world's largest biomass-burning source: TREND IN PARTICLE SSA IN SOUTHERN AFRICA, J. Geophys. Res., 118(12), 6414–6432, doi:10.1002/jgrd.50500, 2013.

560   Flemming, J., and Coauthors, 2017: The CAMS interim Reanalysis of Carbon Monoxide,Ozone and Aerosol for 2003–2015. Atmos. Chem. Phys., 17, 1945–1983, https://doi.org/10.5194/acp-17-1945-2017, 2017.

Formenti, P., D'Anna, B., Flamant, C., Mallet, M., Piketh, S. J., Schepanski, K., Waquet, F., Auriol, F., Brogniez, G. and Burnet, F.: The Aerosols, Radiation and Clouds in southern Africa (AEROCLO-sA) field campaign in Namibia: overview, illustrative observations and way forward, Bull. Am. Met. Soc., 2019.

565   de Graaf, M., Bellouin, N., Tilstra, L. G., Haywood, J. and Stammes, P.: Aerosol direct radiative effect of smoke over clouds over the southeast Atlantic Ocean from 2006 to 2009, Geophysical Research Letters, 41(21), 7723–7730, doi:10.1002/2014GL061103, 2014.

de Graaf, M., Tilstra, L. G. and Stammes, P.: Aerosol direct radiative effect over clouds from synergy of OMI and MODIS reflectance, Atmos. Meas. Tech. Discuss., 2019, 1–21, doi:10.5194/amt-2019-53, 2019a.

570   de Graaf, M., Schulte, R., Peers, F., Waquet, F., Tilstra, L. G. and Stammes, P.: Comparison of south Atlantic aerosol direct radiative effect overclouds from SCIAMACHY, POLDER and OMI/MODIS, Atmos. Chem. Phys. Discuss., 2019, 1–21, doi:10.5194/acp-2019-545, 2019b.

Hagolle, O., Goloub, P., Deschamps, P.-Y., Cosnefroy, H., Briottet, X., Bailleul, T., Nicolas, J.-M., Parol, F., Lafrance, B. and Herman, M.: Results of POLDER in-flight calibration, IEEE transactions on geoscience and 575   remote sensing, 37(3), 1550–1566, 1999.

Halthore, R. N., Eck, T. F., Holben, B. N. and Markham, B. L.: Sun photometric measurements of atmospheric water vapor column abundance in the 940-nm band, J. Geophys. Res., 102(D4), 4343–4352, doi:10.1029/96JD03247, 1997.

Haywood, J. M., Osborne, S. R. and Abel, S. J.: The effect of overlying absorbing aerosol layers on remote sensing 580   retrievals of cloud effective radius and cloud optical depth, Q. J. Royal Met. Soc., 130(598), 779–800, doi:10.1256/qj.03.100, 2004.

Hu, Q., Goloub, P., Veselovskii, I., Bravo-Aranda, J. A., Popovici, I., Podvin, T., Haeffelin, M., Lopatin, A., Pietras, C. and Huang, X.: A study of long-range transported smoke aerosols in the Upper Troposphere/Lower Stratosphere, Atmos. Chem. Phys. Discuss., https://doi. org/10.5194/acp-2018-655, in review, 2018.

585   IPCC, 2013: Climate Change 2013: The Physical Science Basis. Contribution of Working Group I to the Fifth Assessment Report of the Intergovern-mental Panel on Climate Change [Stocker, T.F., D. Qin, G.-K. Plattner, M. Tignor, S.K. Allen, J. Boschung, A. Nauels, Y. Xia, V. Bex and P.M. Midgley (eds.)]. Cambridge University Press, Cambridge, United Kingdom and New York, NY, USA, 1535 pp. 2013.

Kaufman, Y. J. and Fraser, R. S.: The effect of smoke particles on clouds and climate forcing, Science, 277(5332), 590   1636–1639, 1997.

Keil, A. and Haywood, J. M.: Solar radiative forcing by biomass burning aerosol particles during SAFARI 2000: A case study based on measured aerosol and cloud properties, J. Geophys. Res., 108(D13), doi:10.1029/2002JD002315, 2003.

Kirchstetter, T. W., Novakov, T. and Hobbs, P. V.: Evidence that the spectral dependence of light absorption by 595   aerosols is affected by organic carbon, J. Geophys. Res., 109(D21), 2004.

Klopper, D., Formenti, P., Namwoonde, A., Cazaunau, M., Chevaillier, S., Feron, A., Gaimoz, C., Hease, P., Lahmidi, F., Mirande-Bret, C., Triquet, S., Zeng, Z., and Piketh, S. J.: Chemical composition and source apportionment of atmospheric aerosols on the Namibian coast, Atmos. Chem. Phys. Discuss., https://doi.org/10.5194/acp-2020-388, in review, 2020.

600   Kumar, K. R., Sivakumar, V., Reddy, R. R., Gopal, K. R. and Adesina, A. J.: Inferring wavelength dependence of AOD and Ångström exponent over a sub-tropical station in South Africa using AERONET data: Influence of meteorology, long-range transport and curvature effect, Sci. Tot. Environ., 461–462, 397–408, doi:10.1016/j.scitotenv.2013.04.095, 2013.

Lagzi, I., Meszaros, R., Gelybo, G. and Leelossy, A.: Atmospheric chemistry, [online] Available from: 605   http://hgpu.org/?p=11960 (Accessed 6 September 2016), 2014.

Mallet, M., Dulac, F., Formenti, P., Nabat, P., Sciare, J., Roberts, G., Pelon, J., Ancellet, G., Tanré, D., Parol, F. and others: Overview of the Chemistry-Aerosol Mediterranean Experiment/Aerosol Direct Radiative Forcing on the Mediterranean Climate (ChArMEx/ADRIMED) summer 2013 campaign, Atmos. Chem. Phys., 16(2), 455–504, 2016.

610 Mallet, M., Nabat, P., Zuidema, P., Redemann, J., Sayer, A. M., Stengel, M., Schmidt, S., Cochrane, S., Burton, S., Ferrare, R., Meyer, K., Saide, P., Jethva, H., Torres, O., Wood, R., Saint Martin, D., Roehrig, R., Hsu, C. and Formenti, P.: Simulation of the transport, vertical distribution, optical properties and radiative impact of smoke aerosols with the ALADIN regional climate model during the ORACLES-2016 and LASIC experiments, Atmos. Chem. Phys., 19(7), 4963–4990, doi:10.5194/acp-19-4963-2019, 2019.

615 Marenco, F., Johnson, B., Langridge, J. M., Mulcahy, J., Benedetti, A., Remy, S., Jones, L., Szpek, K., Haywood, J., Longo, K. and Artaxo, P.: On the vertical distribution of smoke in the Amazonian atmosphere during the dry season, Atmos. Chem. Phys., 16(4), 2155–2174, doi:10.5194/acp-16-2155-2016, 2016.

McClatchey, R. A.: Optical properties of the atmosphere, Air Force Cambridge Research Laboratories, Office of Aerospace Research, 1972.

620 Meyer, K., Platnick, S. and Zhang, Z.: Simultaneously inferring above-cloud absorbing aerosol optical thickness and underlying liquid phase cloud optical and microphysical properties using MODIS, J. Geophys. Res., 120(11), 5524–5547, 2015.

Myhre, G., Samset, B. H., Schulz, M., Balkanski, Y., Bauer, S., Berntsen, T. K., Bian, H., Bellouin, N., Chin, M., Diehl, T., Easter, R. C., Feichter, J., Ghan, S. J., Hauglustaine, D., Iversen, T., Kinne, S., Kirkevåg, A., Lamarque,
625 J.-F., Lin, G., Liu, X., Lund, M. T., Luo, G., Ma, X., Noije, T. van, Penner, J. E., Rasch, P. J., Ruiz, A., Seland, Ø., Skeie, R. B., Stier, P., Takemura, T., Tsigaridis, K., Wang, P., Wang, Z., Xu, L., Yu, H., Yu, F., Yoon, J.-H., Zhang, K., Zhang, H. and Zhou, C.: Radiative forcing of the direct aerosol effect from AeroCom Phase II simulations, Atmos. Chem. Phys., 13(4), 1853–1877, doi:https://doi.org/10.5194/acp-13-1853-2013, 2013.

Peers, F., Waquet, F., Cornet, C., Dubuisson, P., Ducos, F., Goloub, P., Szczap, F., Tanré, D. and Thieuleux, F.:
630 Absorption of aerosols above clouds from POLDER/PARASOL measurements and estimation of their direct radiative effect, Atmos. Chem. Phys., 15(8), 4179–4196, 2015.

Peers, F., Bellouin, N., Waquet, F., Ducos, F., Goloub, P., Mollard, J., Myhre, G., Skeie, R. B., Takemura, T. and Tanré, D.: Comparison of aerosol optical properties above clouds between POLDER and AeroCom models over the South East Atlantic Ocean during the fire season, Geophysical Research Letters, 43(8), 3991–4000, 2016.

635 Peers, F., Francis, P., Fox, C., Abel, S. J., Szpek, K., Cotterell, M. I., Davies, N. W., Langridge, J. M., Meyer, K. G., Platnick, S. E. and Haywood, J. M.: Observation of absorbing aerosols above clouds over the south-east Atlantic Ocean from the geostationary satellite SEVIRI – Part 1: Method description and sensitivity, Atmos. Chem. Phys., 19(14), 9595–9611, doi:10.5194/acp-19-9595-2019, 2019.

Pelon, J., Flamant, P. H. and Meissonnier, M.: The french airborne backscatter lidar Leandre 1: conception and
640 operation, in Proceedings of the 15th International Laser Radar Conference, Tomsk, USSR, pp. 36–39, Inst. of Atmos. Opt. Tomsk, Russia., 1990.

Pistone, K., Redemann, J., Doherty, S., Zuidema, P., Burton, S., Cairns, B., Cochrane, S., Ferrare, R., Flynn, C., Freitag, S., Howell, S. G., Kacenelenbogen, M., LeBlanc, S., Liu, X., Schmidt, K. S., Sedlacek III, A. J., Segal-Rozenhaimer, M., Shinozuka, Y., Stamnes, S., Diedenhoven, B. van, Harten, G. V. and Xu, F.: Intercomparison
645 of biomass burning aerosol optical properties from in situ and remote-sensing instruments in ORACLES-2016, Atmos. Chem. Phys., 19(14), 9181–9208, doi:https://doi.org/10.5194/acp-19-9181-2019, 2019.

Ramanathan, V. and Carmichael, G.: Global and regional climate changes due to black carbon, Nature Geoscience, 1(4), 221–227, doi:10.1038/ngeo156, 2008.

Redemann, J., Russell, P. B. and Hamill, P.: Dependence of aerosol light absorption and single-scattering albedo
650 on ambient relative humidity for sulfate aerosols with black carbon cores, J. Geophys. Res.: Atmospheres, 106(D21), 27485–27495, doi:10.1029/2001JD900231, 2001.
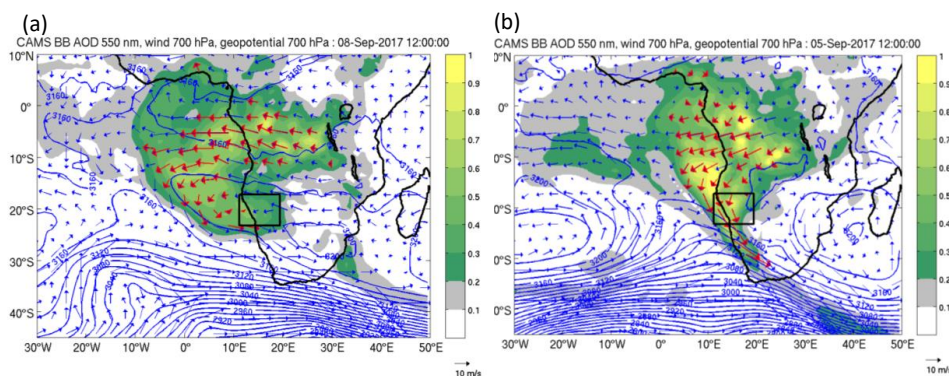
Atmospheric
Chemistry
and Physics
Discussions

Reid, J. S., Eck, T. F., Christopher, S. A., Hobbs, P. V. and Holben, B.: Use of the \AAngstrom exponent to estimate the variability of optical and physical properties of aging smoke particles in Brazil, J. Geophys. Res., 104(D22), 27473–27489, 1999.

655   Rivellini, L.-H., Chiapello, I., Tison, E., Fourmentin, M., Féron, A., Diallo, A., N'Diaye, T., Goloub, P., Canonaco, F. and Prévôt, A. S. H.: Chemical characterization and source apportionment of submicron aerosols measured in Senegal during the 2015 SHADOW campaign., Atmos. Chem. Phys., 17(17), 2017.

Russell, P. B., Bergstrom, R. W., Shinozuka, Y., Clarke, A. D., DeCarlo, P. F., Jimenez, J. L., Livingston, J. M., Redemann, J., Dubovik, O. and Strawa, A.: Absorption Angstrom Exponent in AERONET and related data as an
660   indicator of aerosol composition, Atmos. Chem. Phys., 10(3), 1155–1169, doi:10.5194/acp-10-1155-2010, 2010.

Samset, B. H., Myhre, G., Herber, A., Kondo, Y., Li, S.-M., Moteki, N., Koike, M., Oshima, N., Schwarz, J. P., Balkanski, Y., Bauer, S. E., Bellouin, N., Berntsen, T. K., Bian, H., Chin, M., Diehl, T., Easter, R. C., Ghan, S. J., Iversen, T., Kirkevåg, A., Lamarque, J.-F., Lin, G., Liu, X., Penner, J. E., Schulz, M., Seland, Ø., Skeie, R. B., Stier, P., Takemura, T., Tsigaridis, K. and Zhang, K.: Modelled black carbon radiative forcing and atmospheric
665   lifetime in AeroCom Phase II constrained by aircraft observations, Atmos. Chem. Phys., 14(22), 12465–12477, doi:10.5194/acp-14-12465-2014, 2014.

Schuster, G. L., Dubovik, O. and Holben, B. N.: Angstrom exponent and bimodal aerosol size distributions, J. Geophys. Res., 111(D7), 2006.

Sena, E. T., Artaxo, P. and Correia, A. L.: Spatial variability of the direct radiative forcing of biomass burning
670   aerosols and the effects of land use change in Amazonia, Atmos. Chem. Phys., 13(3), 1261–1275, 2013.

Toledano, C., Cachorro, V. E., Berjon, A., de Frutos, A. M., Sorribas, M., de la Morena, B. A. and Goloub, P.: Aerosol optical depth and Ångström exponent climatology at El Arenosillo AERONET site (Huelva, Spain), Q. J. Royal Met. Soc., 133(624), 795–807, doi:10.1002/qj.54, 2007.

Torres, O., Jethva, H. and Bhartia, P. K.: Retrieval of Aerosol Optical Depth above Clouds from OMI
675   Observations: Sensitivity Analysis and Case Studies, Journal of the Atmospheric Sciences, 69(3), 1037–1053, doi:10.1175/JAS-D-11-0130.1, 2012.

Torres, B., Dubovik, O., Fuertes, D., Schuster, G., Cachorro, V. E., Lapyonok, T., Goloub, P., Blarel, L., Barreto, A. and Mallet, M.: Advanced characterisation of aerosol size properties from measurements of spectral optical depth using the GRASP algorithm, Atmos. Meas. Tech., 10(10), 3743, 2017.

680   Waquet, F., Cornet, C., Deuzé, J.-L., Dubovik, O., Ducos, F., Goloub, P., Herman, M., Lapyonok, T., Labonnote, L. C., Riedi, J. and others: Retrieval of aerosol microphysical and optical properties above liquid clouds from POLDER/PARASOL polarization measurements, Atmos. Meas. Tech., 6(4), 991–1016, 2013a.

Waquet, F., F. Peers, F. Ducos, P. Goloub, S. Platnick, J. Riedi, D. Tanré, and F. Thieuleux: Global analysis of aerosol properties above clouds, Geophys. Res. Lett., 40, 5809–5814, doi:10.1002/2013GL057482, 2013b.
685   Zhang, J., Reid, J. S., Christensen, M. and Benedetti, A.: An evaluation of the impact of aerosol particles on weather forecasts from a biomass burning aerosol event over the Midwestern United States: observational-based analysis of surface temperature, Atmos. Chem. Phys., 16(10), 6475–6494, doi:10.5194/acp-16-6475-2016, 2016.

Zuidema, P., Redemann, J., Haywood, J., Wood, R., Piketh, S., Hipondoka, M. and Formenti, P.: Smoke and Clouds above the Southeast Atlantic: Upcoming Field Campaigns Probe Absorbing Aerosol's Impact on Climate,
690   Bull. Am. Met. Soc., 97(7), 1131–1135, doi:10.1175/BAMS-D-15-00082.1, 2016.
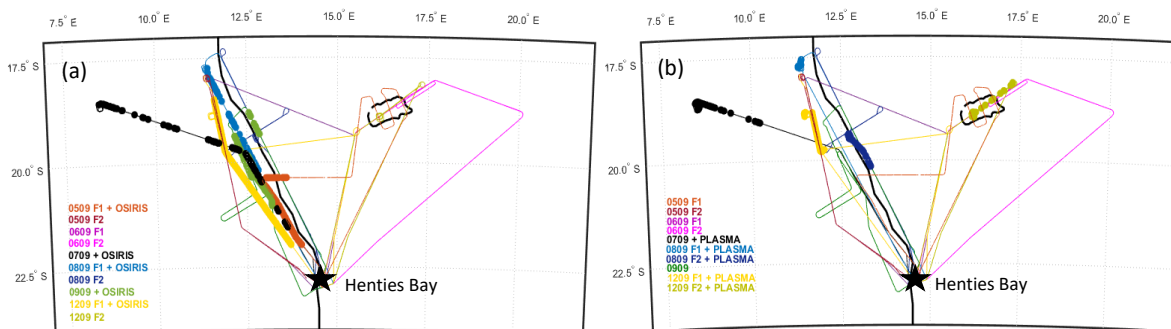
Figure 1: Flight tracks of the 10 flights of the AEROCLO-sA campaign over the Namibian coast in September 2017.
Circles indicate the (a) OSIRIS inversion locations and (b) PLASMA-2 measurement locations at low flight altitudes.

Figure 2: Regional atmospheric circulation and aerosol for a) the 8th of September 2017 and b) the 5th of September
2017 at 12:00 UTC. Geopotential height (contours) and wind (arrows) at 700 hPa and biomass burning AOD at 550
nm (shadings) from CAMS reanalysis are displayed. Red arrows highlight wind vectors at grid points where the AOD
is higher than the 90th percentile of the regional AOD. The AEROCLO-sA campaign region is located with a black
rectangle in the Namibian region.
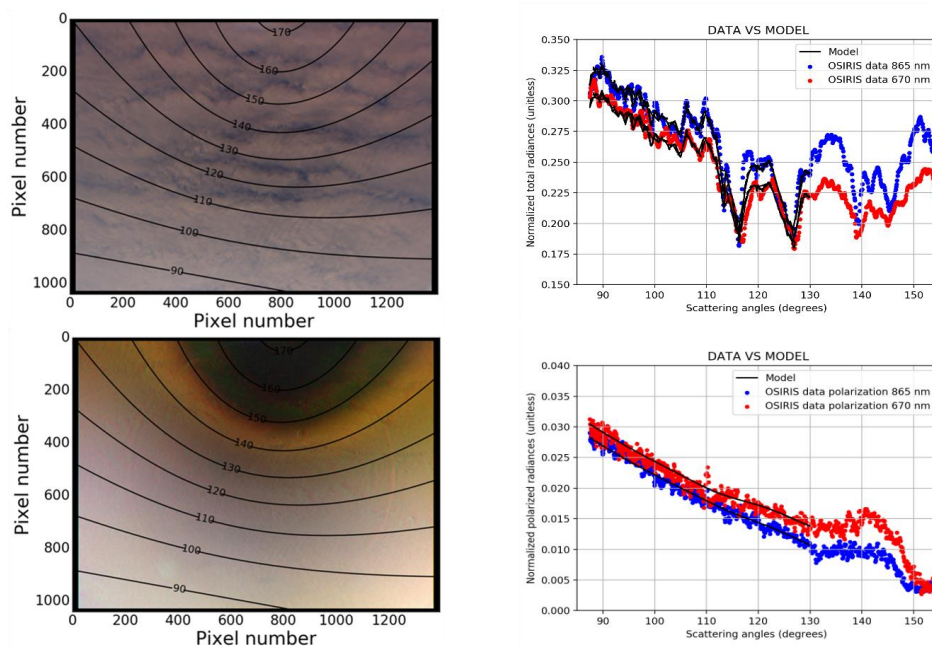
Figure 3: Total and polarised radiances measured by OSIRIS during 12 September 2017. Left panels represent the total, on the top, and the polarised, on the bottom, recomposed RGB radiances for the full OSIRIS image. Right panels represent the corresponding principle planes at 670 nm (red) and 870 nm (blue). OEM's simulations according Waquet et al., (2013) of the total and polarised radiances for scattering angles below 130° are represented with black lines in the right panels.
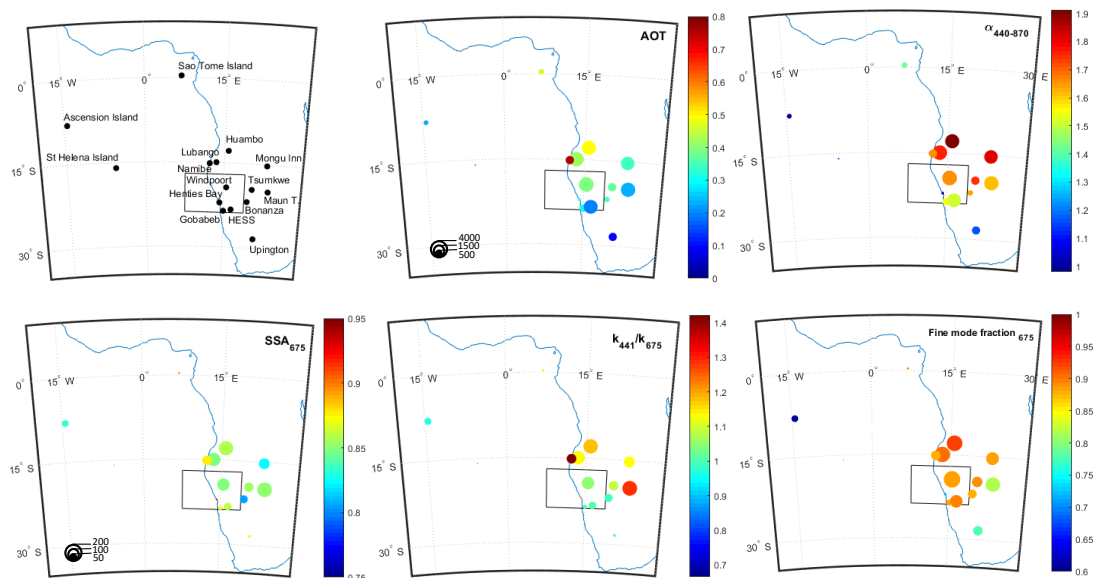
Figure 4: Mean values of AOD at 550 nm, $\alpha_{440-870}$, SSA at 675 nm, ratio of the imaginary part of the refractive index (k) between 441 nm and 675 nm, and the fine to coarse mode fraction of the aerosol volume concentration from 15 AERONET sites in the South-Eastern Atlantic region. The selected period is from the 15 August to the 15 September 2017. The black box corresponds to the AEROCLO-sA flight domain. Circle size is linked to the availability of the data in number of measurements.

16

Atmospheric
Chemistry
and Physics
Discussions
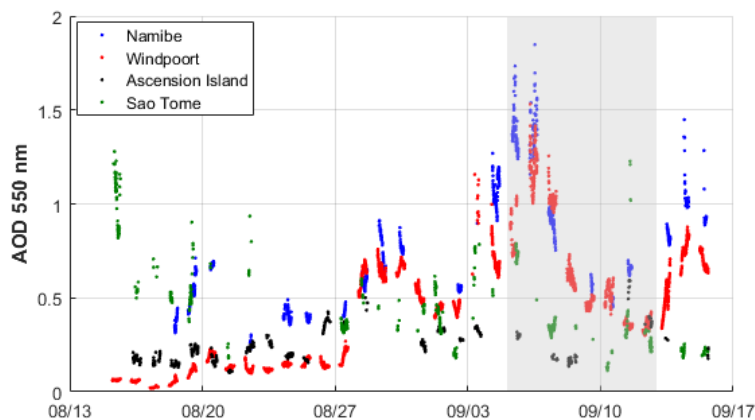
Figure 5: AOD time series measured at 550 nm at Namibe, Windpoort, Ascension Island and Sao Tome AERONET sites from 13 August to 16 September 2017. The grey zone represents the flight period of the AEROCLO-sA campaign.
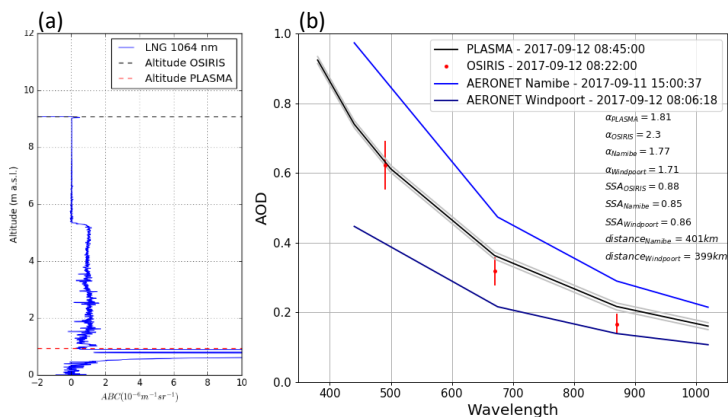

Figure 6: a) Vertical profile of the Aerosol Backscatter Coefficient (ABC) measured at 1064 nm by the airborne lidar LNG before a loop descent performed on 12 September 2017. b) Wavelength dependences of AOD measured at Namibe and Windpoort AERONET ground-based stations, compared to OSIRIS and PLASMA-2 above clouds AODs, estimated before and after the descent in loop. Estimated error bars for AODs are also reported for OSIRIS (red bars) and PLASMA (grey zone).
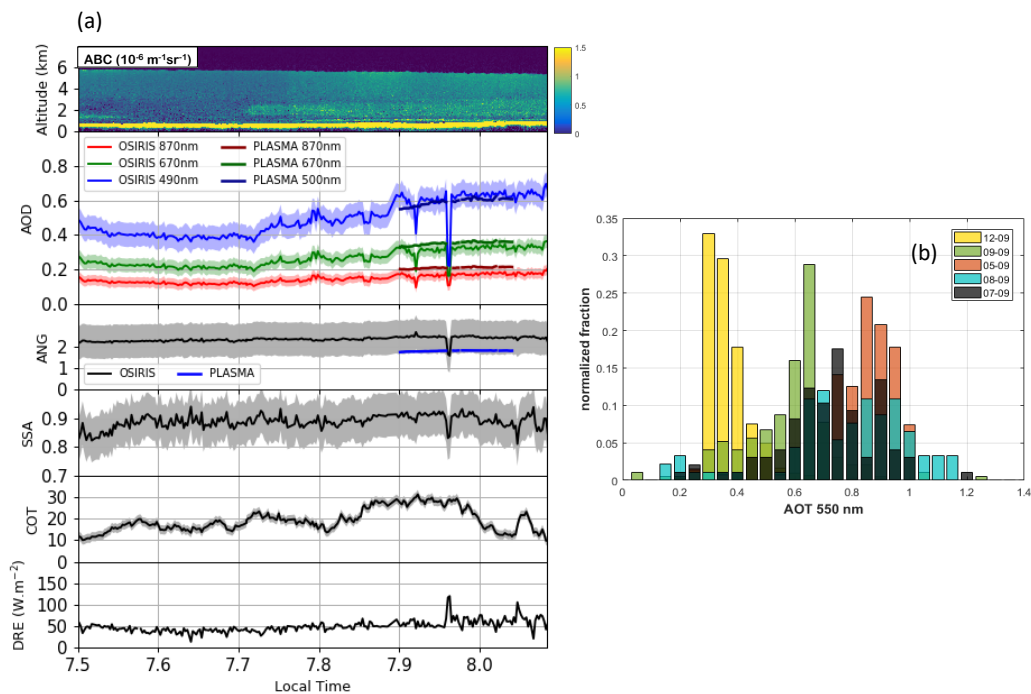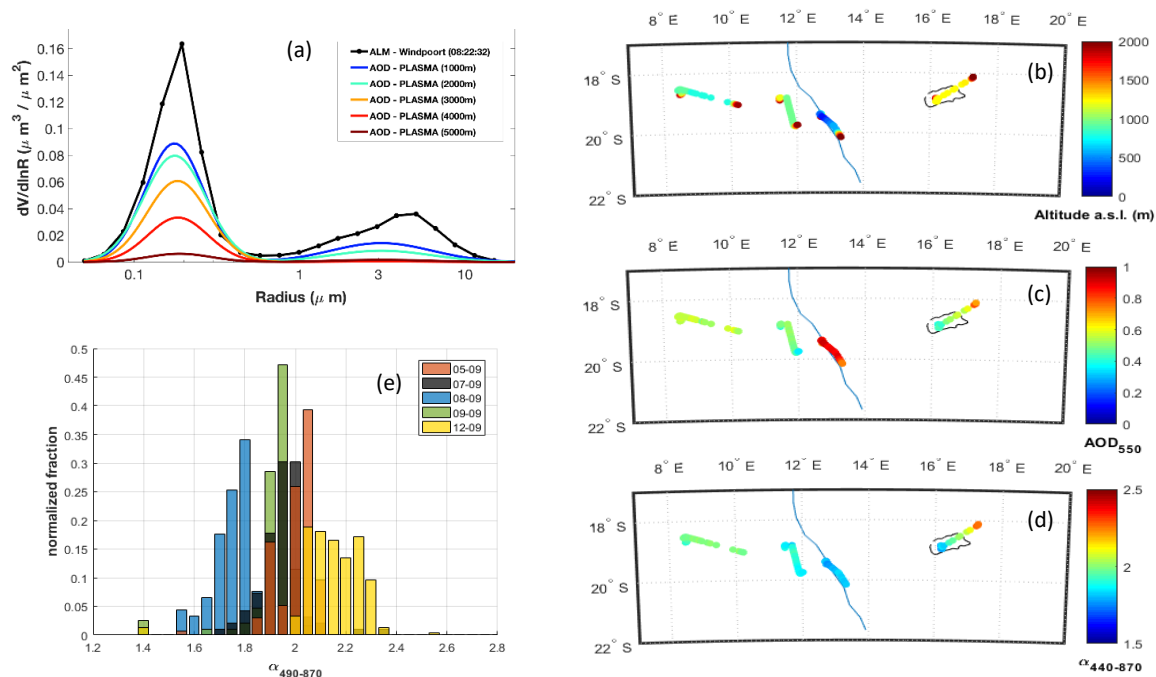
Figure 7: (a) Time series of the ABC profiles measured at 1064 nm by the lidar LNG, above cloud AODs, Angström Exponents (490 nm - 870 nm), aerosol Single Scattering Albedo, Cloud Optical Depth and Direct Radiative Effect estimated on 12 September 2017, and associated errors. (b) AOD histograms for the five selected flights.

700

Figure 8. (a) Retrieved volume particle size distributions at different altitudes from PLASMA2 measurements and from the AERONET station at Windpoort, Namibia, for the descent in loop of the 7 September 2017. Flight altitude **(b)**, AOD **(c)** and Angström exponent **(d)** measured by PLASMA2 during AEROCLO-sA. Only low altitude flights are presented. The black line corresponds to the Etosha Pan. Only low altitude flights are presented. **(e)** Extinction Angström exponent histograms for the five selected flights.
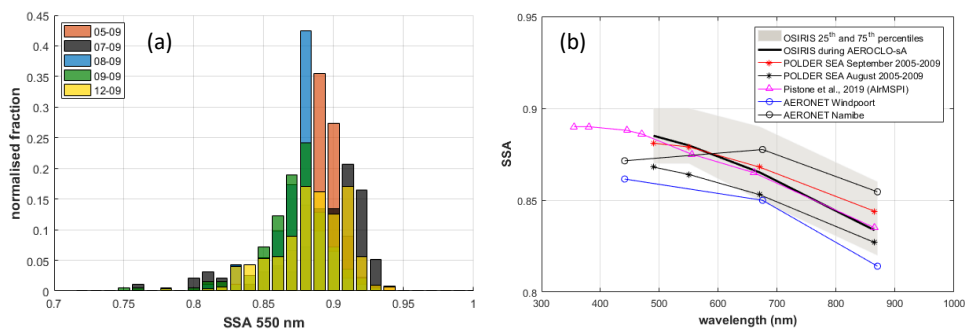
Figure 9: Histogram of the Single Scattering Albedo at 550 nm for the 5 selected flights and mean wavelength dependency retrieved from OSIRIS, Windpoort and Namibe AERONET sites during AEROCLO-sA campaign, AirMSPI during ORACLES campaign in 2016 and POLDER between 2005 and 2009 during the fire season.
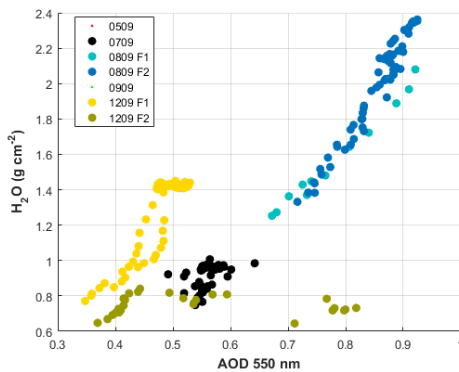
705

Figure 10: Column water vapour in function of AOD at 550 nm both measured by the PLASMA2 Sun-photometer during the AEROCLO-sA campaign.
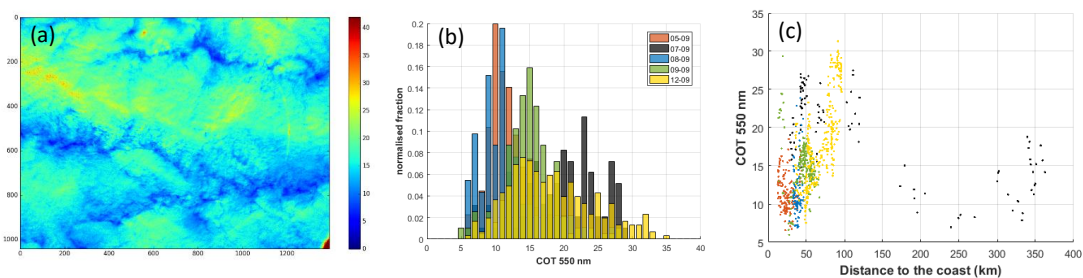

Figure 11: a) Full OSIRIS image Cloud Optical Depth at 550 nm retrieved on 7 September at 09:37 UTC. b) COT histogram for the 5 selected flight. c) Relation between COT and the distance from the measurement to the coastline.
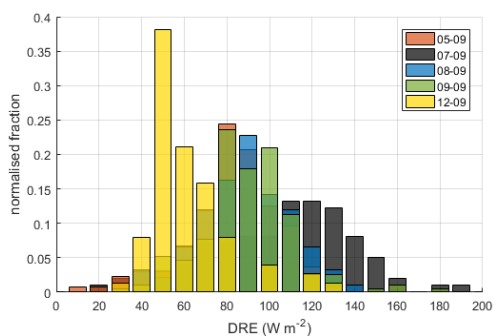
Figure 12: Direct Radiative Effect (DRE) histogram for the 5 selected flights.

Table 1: Aerosol optical properties from AERONET, OSIRIS and PLASMA2 measurements for four different descents in loop during the AEROCLO-sA campaign.

Date	Altitude a.s.l. (m) min/max	AOD_{670} OSIRIS	AOD_{670} PLASMA	AOD_{670} AERONET_Windpoort and distance to F-20	$\alpha_{490-870}$ OSIRIS	$\alpha_{440-870}$ PLASMA	$\alpha_{440-870}$ AERONET_Windpoort
05-09-2017	1244/9650	0.54	0.43	0.55 (373 km)	2.06	1.82	1.76
07-09-2017	900/8680	0.44	0.45	0.75 (745 km)	1.80	1.81	1.66
08-09-2017	686/9050	0.73	0.74	0.50 (464 km)	1.80	1.69	1.66
12-09-2017	940/9080	0.32	0.36	0.22 (399 km)	2.27	1.81	1.71